



LAWRENCE
LIVERMORE
NATIONAL
LABORATORY

Scattering Effects in Passive Foil Focusing of Ion Beams

A. Yuen, S. M. Lund, J. J. Barnard, R. H. Cohen,
J. S. Wurtele

September 14, 2015

Physical Review Special Topics -- Accelerators and Beams

Disclaimer

This document was prepared as an account of work sponsored by an agency of the United States government. Neither the United States government nor Lawrence Livermore National Security, LLC, nor any of their employees makes any warranty, expressed or implied, or assumes any legal liability or responsibility for the accuracy, completeness, or usefulness of any information, apparatus, product, or process disclosed, or represents that its use would not infringe privately owned rights. Reference herein to any specific commercial product, process, or service by trade name, trademark, manufacturer, or otherwise does not necessarily constitute or imply its endorsement, recommendation, or favoring by the United States government or Lawrence Livermore National Security, LLC. The views and opinions of authors expressed herein do not necessarily state or reflect those of the United States government or Lawrence Livermore National Security, LLC, and shall not be used for advertising or product endorsement purposes.

Scattering Effects in Passive Foil Focusing of Ion Beams

Albert Yuen*

*Lawrence Berkeley National Laboratory, Berkeley, CA 94720, USA and
Department of Nuclear Engineering, UC Berkeley, Berkeley, CA 94720, USA*

Steven M. Lund

Facility for Rare Isotope Beams, Michigan State University, East Lansing, MI-48824, USA

John J. Barnard

Lawrence Livermore National Laboratory, Livermore, CA 94550, USA

Ronald H. Cohen

CompX, Del Mar, CA 92014, USA

Jonathan S. Wurtele

*Lawrence Berkeley National Laboratory, Berkeley, CA 94720, USA and
Department of Physics, UC Berkeley, Berkeley, CA 94720, USA*

(Dated: July 31, 2015)

A stack of thin, closely spaced conducting foils has been investigated by Lund et al. [1] as a passive focusing lens for intense ion beams. The foils mitigate space-charge defocusing forces to enable the beam self-magnetic field to focus. In this study, we analyze possible degradation of focusing due to scattering of beam ions resulting from finite foil thickness using an envelope model and numerical simulations with the particle-in-cell code WARP. Ranges of kinetic energy where scattering effects are sufficient to destroy passive focusing are quantified. The scheme may be utilized to focus protons produced in intense laser-solid accelerator schemes. As an example, the spot size of a initially collimated 30 MeV proton beam with initial rms radius $200\text{ }\mu\text{m}$, perveance $Q = 1.8 \times 10^{-2}$, and initial transverse emittance $\varepsilon_{x,\text{rms}} = 0.87\text{ mm mrad}$ propagating through a stack of $6.4\text{ }\mu\text{m}$ thick foils, spaced $100\text{ }\mu\text{m}$ apart, gives a $127.5\text{ }\mu\text{m}$ spot with scattering and a $81.0\text{ }\mu\text{m}$ spot without scattering, illustrating the importance of including scattering effects.

PACS numbers: 29.27.Bd, 41.75.-i, 52.59.Sa

I. INTRODUCTION

Charged particle beams tend to radially expand under space-charge forces and thermal forces if no applied focusing fields constrain their transverse dynamics[2, 3]. Active focusing systems such as solenoids or quadrupole magnets are usually used. However, passive focusing schemes have been investigated which employ material structures to reduce self-fields. These include: Metallic conic guide tubes for electron focusing[4] and ion focusing[5], and stacks of thin foils for electron focusing [6]. Recently, it has been shown that ion beams propagating through a stack of thin metallic foils can be magnetically self-focused due to the mitigation of their electrostatic repulsion[1]. This novel passive focusing scheme opens the possibility of collimating or focusing ion beams to a small spot size since the focusing becomes stronger as the beam radius reduces. Applications may include focusing intense beams on the X-target for fast ignition-driven fusion energy[7], injectors for compact proton accelerators for tumor therapy [8], and ion beam-driven

warm dense matter studies[9]. The stack of thin foils can be made from aluminum and manufactured at low cost. Foil stacks can be used for transverse focusing of laser-produced proton beams[10] where intense space-charge has been limiting applications[11]. This can also remove electrons co-moving with the protons, without large degradations in beam brightness thereby addressing another issue limiting applications. The most studied laser-based ion beam production process, the target-normal-sheath-acceleration (TNSA) model[11], can achieve proton beams with a broad energy spectrum up to a few dozen MeV and whose total current is in the kA range.

Ongoing research based on alternative laser-based ion beam production processes - e.g. radiation pressure acceleration, collisionless shock acceleration, breakout afterburner, acceleration in near-critical and underdense plasmas, resistively enhanced acceleration (see Ref. [10]) - offers beams with promising characteristics (e.g. mono-energetic, higher energy and/or higher current) whose space-charge could be successfully controlled by our stack of thin foils.

An idealized analytical envelope theory was previously developed by Lund et al.[1] and agrees with particle-in-cell simulations. This guided an ongoing campaign of experiments, described in Ref. [12] designed to study the

*ayuen@lbl.gov

mitigation of the defocusing self-electric field of proton beams. These proton beams were produced by intense short-pulse lasers and accelerated by the target-normal-sheath-acceleration (TNSA) process[11] at the TITAN laser facility at GSI and the JUPITER laser facility at Lawrence Livermore National Laboratory[13].

This paper extends the idealized analytical envelope theory of Ref. [1], which assumed infinitely thin foils, to include foil-induced scattering and kinetic energy loss associated with finite thickness foils. This scattering causes random deflections in the distribution of particle angles and results in emittance growth that can degrade beam quality [2, 3, 14, 15]. The beam ions also deposit a fraction of their kinetic energy into the foils, evaporating the foils after penetration of the beam. The stack of foils is therefore a single-use lens. However, estimates show that the foils remain at near solid density during the transit of the beam within the stack because the hydrodynamical expansion timescale is much longer than the beam transit timescale[1, 12]. Besides, the ion beam experiences straggling due to statistical kinetic energy losses into the foils, causing momentum spread and therefore chromatic aberrations as the passive focusing depends on the momentum of the beam ions. Straggling is neglected in our present mono-energetic study: the emphasis is on the angular deflections of the beam ions and the mean kinetic energy loss. Nevertheless, straggling must be taken into account when kinetic energy loss is important. Ref. [1] includes transverse nonlinear effects between the foils in the envelope equations and indicates that modest changes in the radial structure of the beam associated with geometric aberrations do not significantly alter the passive focusing. Numerical simulations (in which the profile is allowed to evolve self-consistently) show reasonably good agreement with these assumptions.

This paper is organized as follows. In Sec. II, foil-induced scattering is treated analytically using the Rutherford scattering model and numerically using the Monte-Carlo particle simulation code SRIM [16]. In Sec. III, the envelope equations are derived and numerically solved for several foil and beam configurations to highlight cases for which foil-induced scattering becomes a dominant limitation of the transverse focusing. In Sec. IV, a module to model foil-induced scattering and kinetic energy loss is implemented in the particle-in-cell code WARP[17] and is applied to numerically test the envelope theory of Sec. III. Good agreement between the envelope theory and numerical model is found.

II. SCATTERING

A. Single particle model

A single beam ion of velocity v_b , charge number Z_b , mass m_b , and kinetic energy $\mathcal{E}_b = (\gamma_b - 1)m_b c^2$, with $\gamma_b = (1 - \beta_b^2)^{-1/2}$, $\beta_b = v_b/c$, and c the speed of light in vacuum, is assumed to penetrate through a homoge-

nous thin foil of thickness Δ_f . The foil is made of a single atomic species of charge number Z_f , mass m_f and mass density ρ_f . The nuclei and electrons of the foil alter the dynamics of the beam ions differently: the electrons can absorb an appreciable amount of energy from the beam ions without causing significant angular deflections, whereas the nuclei absorb little energy but cause significant angular deflections of the beam ions due to their greater electric charge [18]. In this section, the energy loss of the beam ions due to the collisions with atomic electrons is neglected. This is consistent for thin foils with large incident beam kinetic energy [19]. Small kinetic energy losses within one foil are analyzed in Sec. II B. Results found there justify the constant energy assumption.

Because the interaction between the beam ions and the foil nuclei is primarily electrostatic, the differential scattering cross section $d\sigma/d\Omega$ between the incoming beam ion and a stationary foil nucleus, where the solid angle $d\Omega = \sin\theta d\theta d\phi$ (θ is the normal angle, taken as the deflection angle, ϕ is the azimuthal angle in spherical-polar coordinates), is governed by the small-angle Rutherford cross-section[18]

$$\frac{d\sigma}{d\Omega} = \left(\frac{2Z_b Z_f e^2}{4\pi\epsilon_0 m_e c^2} \right)^2 \frac{1 - \beta_b^2}{\beta_b^4} \frac{1}{\theta^4}. \quad (1)$$

Here, e is the elementary electric charge, and ϵ_0 the vacuum permittivity. Here and henceforth, large-angle scattering is ignored: those events are rare[18]. Eq. (1) is valid between a small cutoff angle

$$\theta_{\min} = \frac{\hbar}{p_b a} \simeq \frac{Z_f^{1/3}}{192} \frac{m_e c}{m_b v_b} \quad (2)$$

due to electrostatic screening from bound electrons, and a large cut-off angle

$$\theta_{\max} = \frac{\hbar}{p_b R} \simeq \frac{274}{A_f^{1/3}} \frac{m_e c}{m_b v_b} \quad (3)$$

that is due to the finite radius R of the nucleus. In Eqs. (2) and (3), $a \simeq 1.4a_0 Z_f^{-1/3}$ is the length scale of the screening obtained by a rough fit to the Thomas-Fermi atomic potential, a_0 the Bohr radius, $\hbar = h/(2\pi)$ where h is Planck's constant, A_f is the mass number of the nucleus, m_e is the mass of the electron, and $p_b = m_b v_b$ is the momentum of a assumed non-relativistic beam ion. We approximate $A_f \simeq 2Z_f$.

The total scattering cross-section is

$$\sigma_{\text{tot}} = \int_0^{2\pi} d\phi \int_{\theta_{\min}}^{\theta_{\max}} d\theta \sin\theta \frac{d\sigma}{d\Omega}. \quad (4)$$

A beam ion traversing a thin foil undergoes many small angle deflections and emerges with a small angular deflection due to the cumulative statistical superposition of many small angle collisions. Assuming the number of collisions is sufficient for Gaussian statistics (verified a

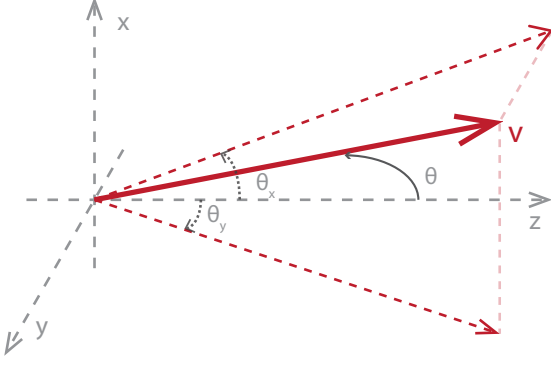


FIG. 1: Schematic of a beam ion at velocity \mathbf{v} that has been deflected by a normal angle θ from the axial direction z . The angular deflections θ_x in the $(x-z)$ plane and θ_y in the $(y-z)$ plane are represented.

posteriori), the central limit theorem applies to the net deflection angle distribution. This implies that the net deflection angle is Gaussian distributed, centered around 0, with variance $\langle \theta^2 \rangle$ given by

$$\langle \theta^2 \rangle \equiv \frac{\int_0^{2\pi} d\phi \int_{\theta_{\min}}^{\theta_{\max}} d\theta \sin \theta \theta^2 \frac{d\sigma}{d\theta}}{\int_0^{2\pi} d\phi \int_{\theta_{\min}}^{\theta_{\max}} d\theta \sin \theta \frac{d\sigma}{d\theta}}. \quad (5)$$

The beam ion undergoes $N = n_f \sigma_{\text{tot}} \Delta_f$ collisions after penetration of a foil of thickness Δ_f and atomic density n_f . Each of these collisions causes a random deflection θ that follows the above-mentioned distribution. We take z as the axial coordinate normal to the foil and x, y as the transverse coordinates. Equation (5) corresponds to a deflection θ_x in the $(x-z)$ plane and a deflection θ_y in the $(y-z)$ plane such that $\theta^2 = \theta_x^2 + \theta_y^2$ in the small angle approximation (see Fig. 1). By symmetry, the mean and the variance of the total deflection angle at foil exit in the $(x-z)$ and the $(y-z)$ plane are therefore 0 and $\langle \theta_{\text{tot}}^2 \rangle \simeq \langle \theta_{x,\text{tot}}^2 \rangle + \langle \theta_{y,\text{tot}}^2 \rangle = 2\langle \theta_{x,\text{tot}}^2 \rangle$ because of symmetry, and with $\langle \theta_{x,\text{tot}}^2 \rangle$ and $\langle \theta_{y,\text{tot}}^2 \rangle$ the variance of total deflection angle at foil exit in the $(x-z)$ and $(y-z)$ planes. If $\beta_b^2 \ll 1$, the rms deflection angle in the $(x-z)$ and $(y-z)$ planes reduce to

$$\langle \theta_{x,\text{tot}}^2 \rangle^{1/2} = \langle \theta_{y,\text{tot}}^2 \rangle^{1/2} = G_0 \frac{\Delta_f^{1/2}}{\mathcal{E}_b}, \quad (6a)$$

$$G_0 = \left[2\pi n_f \left(\frac{Z_b Z_f e^2}{4\pi\epsilon_0} \right)^2 \ln(204 Z_f^{-1/3}) \right]^{1/2}. \quad (6b)$$

The argument in the logarithm in Eq. (6b) depends on the choice of cut-off angle θ_{\min} and θ_{\max} employed which is somewhat arbitrary. However, for our present analysis in which the physics of scattering has been idealized (e.g electron screening is partially omitted), these specific cut-offs are sufficient. What is of interest here is the scaling of the rms deflection angle distribution $\langle \theta_{\text{tot}}^2 \rangle^{1/2}$

in Eq. (6a). The scaling is compared and verified by the Monte-Carlo code SRIM in Sec. II B. The code includes a wider range of physical phenomena (more details can be found in Sec. II B). Eq. (6a) shows that: (i) higher energy beam ions are less likely to be deflected because of their stiffer trajectories, (ii) higher charge states of the beam ions and higher charged foil nuclei yield broader deflections because the Coulomb interaction is stronger, and (iii) ions undergo larger deflections in denser and thicker foils.

B. Monte-Carlo Simulations

The multiple small-angle scattering of beam ions induced by their penetration through a foil is simulated using the Monte-Carlo code SRIM (Stopping and Range of Ions in Matter)[16]. SRIM contains much richer physics than the analytical model used in Sec. II A because it computes the 3D trajectory of a single beam ion through rectangular layers of materials using a quantum mechanical treatment of ion-atom collisions and with adjustments for consistency with experimental data; it also includes screened Coulomb collisions between the beam ion and the foil atoms due to the overlapping electron shells, electron excitations, plasmons, and effective charge Z_f^* effects where $Z_f^* < Z_f$ due to the collective electron cloud, and large angle scattering. Statistical energy losses, angular scattering, kinetic effects related to energy losses from target damage, sputtering, ionization, and phonon production are also accounted for.

SRIM simulation results for protons with three different initial beam kinetic energies, $\mathcal{E}_b = 2$ MeV, 5 MeV and 10 MeV, penetrating a single foil of thickness Δ_f ranging from $0.125 \mu\text{m}$ to $5 \mu\text{m}$ are shown in Figs. 2 and 3. The material of the foil is solid aluminum ($Z_f = 13$, $\rho = 2.7 \text{ g.cm}^{-3}$). For each initial \mathcal{E}_b and Δ_f , $N_p = 3000$ protons ($Z_b = 1$) are tracked and for each proton i , the loss of kinetic energy $\Delta\mathcal{E}_i$ and the deflection angle in the transverse direction $\theta_{\text{tot},i}$ after penetrating the single foil are evaluated. Because of axial symmetry, the deflection angles in both x - and y -directions $\theta_{x,\text{tot},i}$ and $\theta_{y,\text{tot},i}$ are statistically equal. The average of a quantity A is denoted $\langle A \rangle = 1/N_p \sum_{i=1}^{N_p} A_i$ with A_i the individual value for the i -th proton. SRIM also takes into account rare large angle scatterings, which are not relevant for the bulk of the proton distribution. In our averages, we reject protons whose deflection angle at the exit of the foil is more than 5 standard deviations from the mean. We refer to these averages as “smoothed.” We compute, for each initial \mathcal{E}_b and Δ_f , the average kinetic energy loss $\langle \Delta\mathcal{E} \rangle$, the average transverse angular deflection and average squared transverse angular deflection in the x -direction, $\langle \theta_{x,\text{tot}} \rangle$ and $\langle \theta_{x,\text{tot}}^2 \rangle$, and in the y -direction, $\langle \theta_{y,\text{tot}} \rangle$ and $\langle \theta_{y,\text{tot}}^2 \rangle$.

The smoothed average kinetic energy loss $\langle \Delta\mathcal{E} \rangle$, as a function of foil thickness Δ_f , is plotted in Fig. 2. As expected, $\langle \Delta\mathcal{E} \rangle$ is small for small Δ_f and high \mathcal{E}_b . In the case where $\mathcal{E}_b = 5$ or 10 MeV, protons lose a negligible

amount of their initial kinetic energy (2% or less), even for foils up to 5 μm . However, the 2 MeV protons lose close to 8% of their kinetic energy after penetrating 5 μm of solid aluminum. The assumption of constant kinetic energy for beam protons becomes relatively poor for μm thick foils with a proton energy lower than 2 MeV. Although the proton kinetic energy can be taken to be constant within one foil, it cannot be assumed to be constant in the full stack of foils because the small decrements in kinetic energy in each foil can result in a substantial net total energy loss when penetrating many foils.

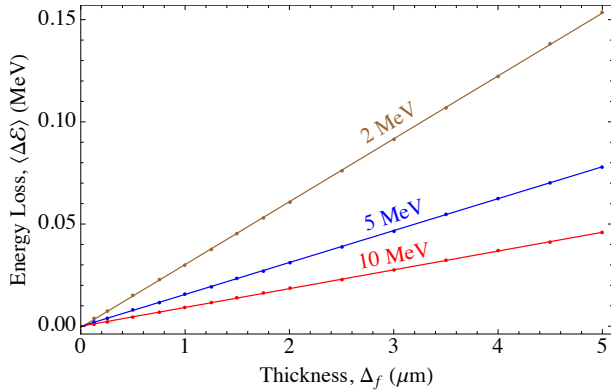


FIG. 2: (Color) Dots give smoothed (large angle events rejected) proton kinetic energy loss computed with SRIM, averaged over $N_p = 3000$ protons with initial kinetic energy \mathcal{E}_b as indicated after penetration of a solid aluminum foil of thickness Δ_f . Smoothing eliminates less than 0.2% of the simulated protons in the worst case with $\mathcal{E}_b = 2$ MeV and $\Delta_f = 5 \mu\text{m}$. Solid lines correspond to a linear fit of the data for initial kinetic energies \mathcal{E}_b . Brown, blue and red colors represent initial kinetic energies $\mathcal{E}_b = 2, 5$ and 10 MeV.

As expected, there is zero mean angular deflection: $\langle \theta_{x,\text{tot}} \rangle = \langle \theta_{y,\text{tot}} \rangle = 0$ (plot not shown). The rms deflection angle $\langle \theta_{x,\text{tot}}^2 \rangle^{1/2} (= \langle \theta_{y,\text{tot}}^2 \rangle^{1/2})$ because of symmetry) as a function of foil thickness Δ_f from the smoothed distribution is plotted in Fig. 3. A least-square fit based on the Δ_f and \mathcal{E}_b dependance of Eq. (6) and the results of the Monte-Carlo simulations shows that

$$\langle \theta_{x,\text{tot}}^2 \rangle^{1/2} = G_{\text{SRIM}} \frac{\Delta_f^{1/2}}{\mathcal{E}_b}, \quad (7)$$

with $G_{\text{SRIM}} = 9.8 \times 10^{-3} \text{ MeV} \mu\text{m}^{-1/2}$. In contrast, using $Z_b = 1$, $Z_f = 13$ and $n_f = 6.02 \times 10^{28} \text{ m}^{-3}$, the coefficient G_0 from Eq. (6) gives $G_0 = 2.4 \times 10^{-2} \text{ MeV} \mu\text{m}^{-1/2}$ for aluminum which is 2.4 times higher than G_{SRIM} . Such a discrepancy may be justified by the richer models that SRIM employed compared to the model in Sec. II A. Equation (7), is employed in the analysis in the following sections since it should be more accurate. Note also that for $\mathcal{E}_b = 5$ MeV and 10 MeV, Eq. (7) produces an excellent fit to the SRIM simulation results. In contrast, data slightly departs from the fit for 2 MeV, because the significant loss of kinetic energy for lower energy protons results in enhanced angular scattering.

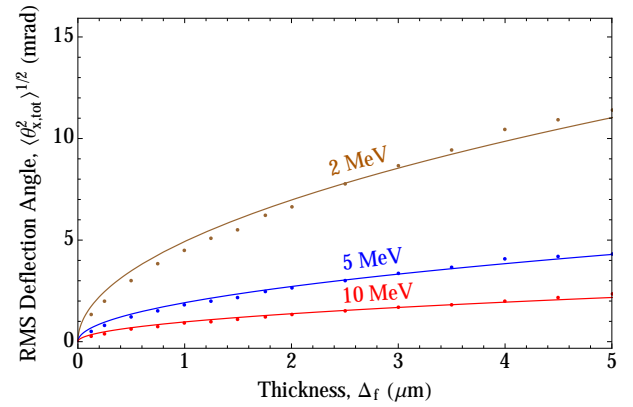


FIG. 3: (Color) Dots give smoothed (large angle events rejected) rms deflection angle computed with SRIM, averaged over $N_p = 3000$ protons with initial ion kinetic energy \mathcal{E}_b after penetration of a solid aluminum foil of thickness Δ_f . Solid lines correspond to fits of the data based on Eq. (6) using a least-squared method for each initial kinetic energy \mathcal{E}_b . Brown, blue and red colors respectively represent the initial kinetic energies of $\mathcal{E}_b = 2, 5$ and 10 MeV.

Methods presented in this section using SRIM can be readily applied to other foil materials and a variety of incident ions.

III. TRANSVERSE ENVELOPE MODEL

This section closely follows the treatment in Ref. [1]. First, the beam model, the geometry of the foil system, and the beam fields are described, and then, particle equations of motion both between two foils and within a foil are derived. The particle equations of motion are averaged to obtain an envelope equation for the transverse beam radius. Illustrative examples of scattering effects on beam propagation are presented in Sec. III E.

A. Geometry and Beam Model

The focusing system (see Fig. 4) is treated as a two-foil system separated by length L , perpendicular to the axial z axis, centered at $z = 0$ and infinite in the transverse directions x and y . This model requires that the characteristic transverse beam radius is much smaller than the transverse extent of the foils. Each foil has finite thickness Δ_f : the beam dynamics is therefore treated differently between the foils and within a foil. The foils are assumed to be grounded conductors.

The ion beam is assumed to be single-species, mono-energetic with kinetic energy \mathcal{E}_b , mass m_b and charge $q = Z_b e$, filling the space between many foils. The axial extent of the beam is assumed to be long compared to its transverse size. We describe the beam with a Vlasov model and beam distribution function $f_b(\mathbf{x}_\perp, \mathbf{p}, z)$. Be-

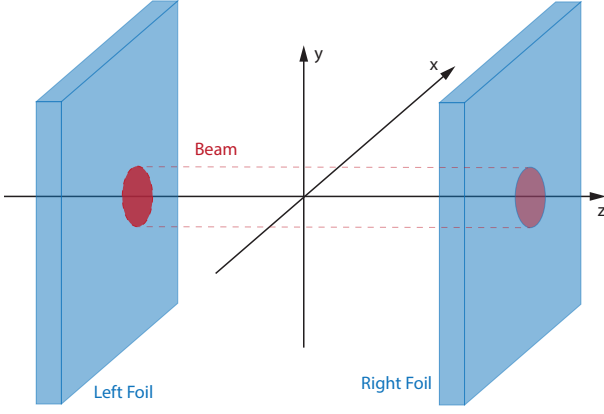


FIG. 4: (Color) Axisymmetric beam between two conducting foils located at $z = \pm L/2$. The foils are grounded.

cause the beam is assumed mono-energetic, the axial coordinate z can be chosen as an independent variable, in place of the time t .

The beam charge density $\rho_b = q \int d^3p f_b$ is assumed to be axisymmetric ($\partial \rho_b / \partial \theta = 0$). The z -variation of ρ_b is neglected between two adjacent foils and within a foil, i.e. $\rho_b = \rho_b(r)$, where $r = \sqrt{x^2 + y^2}$. However, $\rho_b(r)$ is assumed to vary with z on length scales larger than the inter-foil spacing.

The beam line charge $\lambda_b = 2\pi \int_0^{+\infty} dr r \rho_b(r)$ is proportional to the beam current I_b with $I_b = \beta_b c \lambda_b$. By definition, the beam current density is $\mathbf{J}_b = q \int d^3p \mathbf{v} f_b$ with \mathbf{v} the particle velocity. The beam is assumed to be mostly axial, $\mathbf{J}_b \simeq \hat{\mathbf{z}} \beta_b c \rho_b(r)$. Here, $\beta_b c$ is the axial beam velocity consistent with the axial particle energy $\mathcal{E}_b = (\gamma_b - 1)mc^2$ where $\gamma_b = 1/\sqrt{1 - \beta_b^2}$. The radial shape of the charge density ρ_b is assumed not to change form throughout the stack of foils (in z) while the radial extent of the beam charge density is allowed to vary in z . This idealization of self-similar evolution is consistent with the conservation of the linear charge density ($\lambda = \text{const.}$) under radial self-field forces[1].

The transverse (\perp) statistical average of a quantity A over the beam distribution $f_b(\mathbf{x}, \mathbf{p}, z)$ is defined by

$$\langle A \rangle_{\perp} \equiv \frac{\int d^2x_{\perp} \int d^3p A(\mathbf{x}_{\perp}, \mathbf{p}, z) f_b}{\int d^2x_{\perp} \int d^3p f_b}, \quad (8)$$

where $\mathbf{x}_{\perp} = \hat{\mathbf{x}}x + \hat{\mathbf{y}}y$ denotes the transverse coordinate. The z -varying radial extent of the beam charge density is measured by the rms width $\sigma_x(z) \equiv \langle x^2 \rangle_{\perp}^{1/2}$.

B. Self-field solutions

In this section, the beam electric and magnetic fields are explicitly solved for the case of an axisymmetric beam profile. We employ the quasi-static approximation: $\partial \mathbf{E} / \partial t \simeq 0$ and $\partial \mathbf{B} / \partial t \simeq 0$ in Maxwell's equations. The boundary conditions are set by the conducting foils. E_r

is screened by the conducting foils: $E_r = 0$ within the foils, and B_{θ} remains unmodified by the foils. Details of the derivations can be found in Ref. [1].

a. Self-magnetic field between two foils Using a potential vector \mathbf{A} such that $\mathbf{B} = \nabla \times \mathbf{A}$ and the Coulomb gauge $\nabla \cdot \mathbf{A} = 0$, $\mathbf{A} \simeq \hat{\mathbf{z}} A_z$ and $\nabla^2 A_z \simeq -\mu_0 \beta_b c \rho_b(r)$. Here, μ_0 is the permeability of free space and $c^2 = 1/(\mu_0 \epsilon_0)$. \mathbf{E} can be expressed as the gradient of an electrostatic potential in vacuum ϕ_v such that $\nabla^2 \phi_v = -\rho_b(r)/\epsilon_0$. The integration of the two previous equations using relevant radial boundary conditions yield $A_z(r) \simeq \beta_b \phi_v(r)/c$. The self-magnetic field has therefore only an azimuthal component

$$\mathbf{B} \simeq \hat{\boldsymbol{\theta}} B_{\theta}(r) \simeq -\hat{\boldsymbol{\theta}} \frac{\beta_b}{\epsilon_0 c r} \int_0^r d\tilde{r} \tilde{r} \rho_b(\tilde{r}). \quad (9)$$

b. Self-magnetic field within a foil As the thickness of the foils Δ_f is small compared to the inter-foil spacing L ($\Delta_f/L \ll 1$), \mathbf{B} is assumed constant and equal to the self-magnetic field at the surface of the foils.

c. Self-electric field between two foils \mathbf{E} can be expressed as the gradient of an electrostatic potential ϕ_g such that $\mathbf{E} = -\nabla \phi_g$ and

$$\nabla^2 \phi_g = -\frac{\rho_b(r)}{\epsilon_0}. \quad (10)$$

In contrast to ϕ_v , ϕ_g takes into account the boundary values $\phi_g = 0$ on the foils at $z = \pm L/2$. Ref. [1] provides the derivation of the solution to Eq. (10):

$$\begin{aligned} \phi_g(r, z) = & \frac{1}{\epsilon_0} \int_0^{\infty} \frac{dk}{k} \frac{\cosh(kL/2) - \cosh(kz)}{\cosh(kL/2)} J_0(kr) \\ & \times \int_0^{\infty} d\tilde{r} \tilde{r} \rho_b(\tilde{r}) J_0(k\tilde{r}). \end{aligned} \quad (11)$$

Here, J_0 denotes a 0th order ordinary Bessel function. It was found in Ref. [1] that the radial $E_r = -\partial \phi_g / \partial r$ and axial $E_z = -\partial \phi_g / \partial z$ field components could, to a good approximation, be replaced by the z -average values between the foils

$$\begin{aligned} \overline{E}_{r,g}(r) &= \int_{-L/2}^{L/2} \frac{dz}{L} E_r(r, z) \\ &= \frac{1}{\epsilon_0} \int_0^{\infty} dk \left[1 - \frac{2}{kL} \tanh(kL/2) \right] J_1(kr) \\ &\quad \times \int_0^{\infty} d\tilde{r} \tilde{r} \rho_b(\tilde{r}) J_0(k\tilde{r}), \\ \overline{E}_{z,g}(r) &= \int_{-L/2}^{L/2} \frac{dz}{L} E_z(r, z) = 0. \end{aligned} \quad (12)$$

d. Self-electric field within a foil The foils are assumed to be perfect conductors so that $\mathbf{E} = 0$.

C. Particle Dynamics

The particle dynamics between the thin foils has been previously treated[1]. This section extends the analysis to include the deleterious effects of scattering within a foil.

The particle dynamics is analyzed in two separate regions: between two foils, which is assumed to be vacuum, and within a perfectly conducting foil. Intra-beam scattering is neglected. Within a foil, deflections of beam ions due to the scattering with foil atoms are included in the equations of motion using the results of Sec. II. A static magnetic field can also be superimposed to improve focusing as treated in Ref. [1].

Between two foils The beam charge density is assumed to be axisymmetric, and the foils are assumed to be transversely homogenous, leading to axisymmetric self-fields. The axial self-electric field, $E_z(r, z)$, is neglected. In the paraxial approximation ($\mathbf{v} = \hat{\mathbf{z}}\beta_b c + \delta\mathbf{v} \simeq \hat{\mathbf{z}}\beta_b c$), the single particle equation of motion between the foils is

$$\mathbf{x}_\perp'' \simeq \frac{q}{m\gamma_b c^2} \frac{\partial \phi_v}{\partial \mathbf{x}_\perp} - \frac{q}{m\gamma_b \beta_b^2 c^2} \frac{\partial \phi_g}{\partial \mathbf{x}_\perp}. \quad (13)$$

Here, derivatives with respect to z are represented by primes ($' = d/dz$). The first term on the right-hand side of Eq. (13) represents the self-magnetic focusing contribution, and the second term corresponds to the self-electric defocusing contribution.

Within a foil Because the foils are assumed to be perfect conductors, no electric field penetrates the foils. The finite thickness of the foils induces Coulomb scattering between beam ions and foil atoms. Therefore, beam ions are both transversely deflected and lose kinetic energy on the foils.

Knock-on electrons emitted from the foils[20] and their effects on the dynamics of the beam ions are a topic for further research. Knock-on electrons fill the gaps between the foils, and the subsequent current neutralization is greater than the subsequent charge neutralization as, by definition, the velocity of the knock-on electrons is higher than the ion beam velocity. Knock-on electrons could therefore mitigate the passive focusing scheme. Nevertheless, the presence of knock-on electrons does not confound the passive focusing in regimes where the foil atoms and the beam ions are of low atomic number, where the beam kinetic energy is high, and where the foils are thin. In this case, the number of generated knock-on electrons would remain negligibly low according to the Rutherford scattering model.

The ion beam kinetic energy \mathcal{E}_b is no longer constant and depends on the distance travelled within the foil and the stopping power \mathcal{S} of the foil material. Values of \mathcal{S} are found in tabulated data such as the PSTAR database[21]. Straggling is ignored here, where we consider transverse dynamics. An analysis of straggling would be important for substantial changes in mean beam energy or when

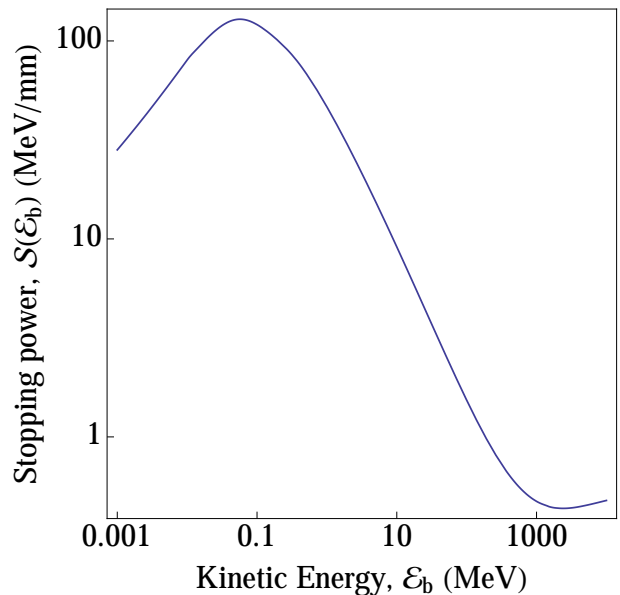


FIG. 5: Stopping power $\mathcal{S}(\mathcal{E}_b)$ of a proton in solid aluminum (mass density $\rho = 2.7\text{g/cm}^3$).

energy spread is important. The electric field vanishes in the foil, and terms representing energy loss and the scattering-induced deflection of the particle are added. The cumulative scattering-induced deflection of a single particle trajectory is a stochastic process that depends on the distance z travelled in the material and the material properties. It is modeled by a Brownian noise w such that for $0 \leq z_0 \leq z \leq \Delta_f$, $w(z) - w(z_0)$ is a Gaussian distributed variable with mean 0 and variance $(z - z_0) \times G^2/\mathcal{E}_b^2(z)$ to have a form consistent with Eqs. (6) and (7). The instantaneous scattering-induced deflection in the particle equation of motion is therefore represented by the white noise w' which is the formal derivative of the Brownian noise w . The equation of motion is then the stochastic differential equation

$$\mathbf{x}_\perp'' + \frac{(\gamma_b \beta_b)'}{(\gamma_b \beta_b)} \mathbf{x}_\perp' - \frac{q}{m\gamma_b c^2} \frac{\partial \phi_v}{\partial \mathbf{x}_\perp} \simeq w', \quad (14)$$

and includes the particle kinetic energy loss due to the stopping power of the foil material $\mathcal{E}_b' = \mathcal{S}(\mathcal{E}_b)$ (see Fig. 5), or equivalently

$$(\gamma_b \beta_b)' = \frac{\mathcal{S}(\mathcal{E}_b)}{mc^2 \beta_b}. \quad (15)$$

The deceleration-induced term $\frac{(\gamma_b \beta_b)'}{(\gamma_b \beta_b)} \mathbf{x}_\perp'$ is derived in Ref. [3].

D. Envelope equations

The statistical transverse envelope equations are derived by taking the derivatives in z of $\sigma_x(z)$

and the transverse rms emittance of the beam $\varepsilon_{x,\text{rms}} \equiv [\langle x^2 \rangle_\perp \langle x'^2 \rangle_\perp - \langle xx' \rangle_\perp^2]^{1/2}$, and then applying the particle equations between two foils and within one foil. Because the beam is axisymmetric, only the x -component of the beam envelope equation is treated. This section extends the envelope formalism of Ref. [1] to include additional effects due to scattering within a foil.

Between two foils The beam envelope equation between two foils, derived in Ref. [1], is

$$\frac{d^2}{dz^2} \sigma_x + \frac{\gamma_b^2}{4} [\beta_b^2 - \bar{F}] \frac{Q}{\sigma_x} - \frac{\varepsilon_{x,\text{rms}}^2}{\sigma_x^3} = 0. \quad (16)$$

The dimensionless perveance $Q = q\lambda_b/(2\pi\epsilon_0 m\gamma_b^3 \beta_b^2 c^2)$ is constant[2, 3, 22]. It is assumed that, between the foils, the nonlinear field effects are small and therefore $\varepsilon_{x,\text{rms}}$ is constant.

$$\bar{F} = -\frac{4\pi\epsilon_0}{\lambda} \langle r \int_{-L/2}^{L/2} \frac{dz}{L} \frac{\partial \phi_g}{\partial r} \rangle_\perp \quad (17)$$

is a dimensionless “form factor” that models the average screening of the defocusing field due to the foils for closely spaced foils ($L \ll \rho(\partial\rho/\partial z)^{-1}$) as the beam ions cannot rapidly respond to fast variations of the defocusing electric field between closely spaced foils (see Ref. [1] for details). Scattering does not change this result as it does not happen between the foils. In vacuum, $\bar{F} = 1$ and the envelope equation reduces to the familiar vacuum form[1]. The form factor $\bar{F} \in [0, 1]$ can be effectively seen as an attenuation factor of the defocusing electric field due to the foils.

Within a single foil In this paragraph, $z = 0$ is taken at the middle of the foil and the foil domain in z is $[-\Delta_f/2, \Delta_f/2]$. Equation (14) and the derivatives of $\langle x^2 \rangle_\perp^{1/2}$ in z yield the beam envelope equation within a single foil.

$$\begin{aligned} \frac{d^2}{dz^2} \sigma_x + \frac{(\gamma_b \beta_b)'}{(\gamma_b \beta_b)} \frac{d}{dz} \langle xx' \rangle_\perp^{1/2} \\ + \frac{\gamma_b^2}{4} \beta_b^2 \frac{Q}{\sigma_x} - \frac{\varepsilon_{x,\text{rms}}^2}{\sigma_x^3} = \frac{\langle xw' \rangle_\perp}{\sigma_x}. \end{aligned} \quad (18)$$

Equation (18) differs from the beam envelope equation between two foils, Eq. (16), by the absence of a defocusing electric field, and the presence of scattering and deceleration. Furthermore, the emittance is not conserved because of both kinetic energy losses and cross-terms between x , x' and w' due to scattering-induced deflections. Differentiating $\varepsilon_{x,\text{rms}}^2$ with respect to z and applying Eq. (14) yields

$$\frac{d}{dz} \varepsilon_{x,\text{rms}}^2 = -2 \frac{(\gamma_b \beta_b)'}{\gamma_b \beta_b} \varepsilon_{x,\text{rms}}^2 + 2\sigma_x^2 \langle x'w' \rangle_\perp - 2\langle xx' \rangle_\perp \langle xw' \rangle_\perp. \quad (19)$$

In Appendix A, a detailed analysis of the cross-terms for beam kinetic energy \mathcal{E}_b leads to Eqs. (A10) and (A13), and shows that $\langle xw' \rangle_\perp = 0$ and $\langle x'w' \rangle_\perp = G^2/(2\mathcal{E}_b^2)$. Using these results, Eq. (18) reduces to

$$\frac{d^2}{dz^2} \sigma_x + \frac{(\gamma_b \beta_b)'}{\gamma_b \beta_b} \frac{d}{dz} \langle xx' \rangle_\perp^{1/2} + \frac{\gamma_b^2}{4} \beta_b^2 \frac{Q}{\sigma_x} - \frac{\varepsilon_{x,\text{rms}}^2}{\sigma_x^3} = 0, \quad (20)$$

and Eq. (19) reduces to

$$\frac{d}{dz} \varepsilon_{x,\text{rms}}^2 = -2 \frac{(\gamma_b \beta_b)'}{\gamma_b \beta_b} \varepsilon_{x,\text{rms}}^2 + \frac{G^2}{\mathcal{E}_b^2} \sigma_x^2. \quad (21)$$

For a paraxial beam, angles of particle trajectories in the foil are small and the total distance travelled by the ions within the foil is, therefore, to first approximation, Δ_f . The beam size can be approximated as constant within an individual foil ($\sigma_x = \text{const}$) when the foils are thin compared to transverse focal length. Then, the kinetic energy loss $\Delta\mathcal{E}_b$ of the ion beam reduces to

$$\Delta\mathcal{E}_b \simeq \mathcal{S}(\mathcal{E}_b(-\Delta_f/2))\Delta_f \simeq \mathcal{S}(\mathcal{E}_b)\Delta_f. \quad (22)$$

Generally, $|\Delta\mathcal{E}_b| \ll \mathcal{E}_b$, and the energy \mathcal{E}_b can be assumed constant within a single foil when computing quantities that are functions of \mathcal{E}_b because the higher-order induced errors are small. The emittance evolution equation (19) can then be integrated across a foil,

$$\begin{aligned} \varepsilon_{x,\text{rms}}^2(\Delta_f/2) &= \varepsilon_{x,\text{rms}}^2(-\Delta_f/2) + \int_{-\Delta_f/2}^{\Delta_f/2} dz \frac{d}{dz} \varepsilon_{x,\text{rms}}^2(z) \\ &\simeq \varepsilon_{x,\text{rms}}^2(-\Delta_f/2) \\ &\quad + \Delta_f \left[-2 \frac{(\gamma_b \beta_b)'}{\gamma_b \beta_b} \varepsilon_{x,\text{rms}}^2 + \frac{G^2}{\mathcal{E}_b^2} \sigma_x^2 \right]_{z=-\Delta_f/2}. \end{aligned} \quad (23)$$

In Eq. (23), terms of order Δ_f^2 and higher are neglected. Because the foils induce deceleration of the ions, $(\gamma_b \beta_b)'$ is negative, causing emittance growth. Because G is always positive, the scattering term also causes emittance growth. Note that while the kinetic energy loss within one foil is small compared to the kinetic energy of the beam, the accumulated losses of kinetic energy due to its propagation through a large number of foils can be significant and should be accounted in the beam dynamics. We employ the thin foil approximation and apply Eqs. (22) and (23) in the following sections.

Note that, instead of our previously defined transverse emittance, it is possible to use the normalized transverse emittance as a measure of beam quality as it is a conserved quantity under acceleration or deceleration. In this case, an auxiliary equation for γ_b' [3] must be taken into account.

E. Example: Application of the envelope model to intense proton beams

We analyze a lens where thin foils of constant thickness Δ_f are stacked with constant foil spacing L . Mod-

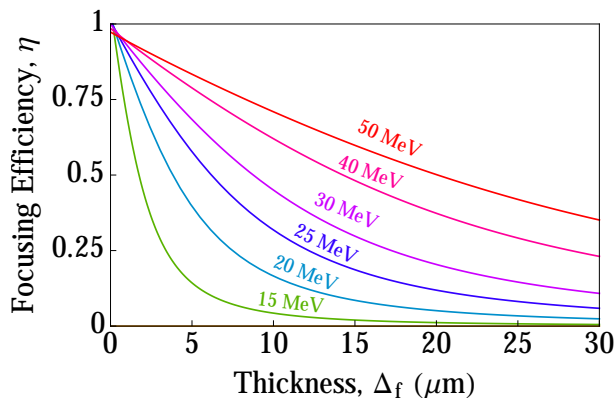


FIG. 6: (Color) Proton focusing efficiency η as a function of foil thickness Δ_f is computed for specified initial kinetic energies \mathcal{E}_b . Green, cyan, blue, purple, pink, red colors represent initial kinetic energies $\mathcal{E}_b = 15, 20, 25, 30, 40$ and 50 MeV.

TABLE I: Minimum $\sigma_{x,\min}$ and corresponding z -location z_{\min} (effective focal length) for foil spacing $L = 100 \mu\text{m}$ and initial kinetic energy $\mathcal{E}_b = 30$ MeV for different foil thicknesses Δ_f . Corresponding focusing efficiency η , kinetic energy \mathcal{E}_b at $\sigma_{x,\min}$, and beam rms emittance growth $\Delta\epsilon_{x,\text{rms}}$ at $\sigma_{x,\min}$ are displayed for the 30 MeV initial beam shown in Fig. 6 and 7.

Foil Thickness Δ_f (μm)	Foil Spacing $L = 100 \mu\text{m}$				
	$\sigma_{x,\min}$ (μm)	η	z_{\min} (mm)	\mathcal{E}_b (MeV)	$\Delta\epsilon_{x,\text{rms}}$ (mm mrad)
0	81.0	1	19.0	30	0
1.6	94.1	0.89	19.1	28.8	0.4
3.2	106.1	0.79	19.0	27.7	0.7
6.4	127.5	0.61	18.4	25.4	1.2
12.8	157.6	0.36	16.1	22.1	2.1

ulation of foil spacing L as a function of the beam radial size can optimize the focusing mechanism, but is not treated here. The foil material is solid aluminum ($\rho = 2.7 \text{ g.cm}^{-3}$, $Z_f = 13$), with angular deflection coefficient $G_{\text{SRIM}} = 9.8 \times 10^{-3} \text{ MeV}\mu\text{m}^{-1/2}$ from Sec. II and the stopping power $\mathcal{S}(\mathcal{E}_b)$ extracted from Ref. [21]. Use of conducting materials different from solid aluminum results in a different deflection coefficient G that can be recomputed using the methods of Sec. II, and a different stopping power $\mathcal{S}(\mathcal{E}_b)$. The continuous approximation of the form factor \bar{F} from Eq. (17) is used. No external focusing system is employed. The ion beam is assumed to have no angular momentum. Secondary electrons and neutralizing plasma are neglected.

For efficient passive focusing, the beam must ideally be high current and high energy consistently as analyzed in Sec. IIID. For example, consider a proton beam with a high perveance value of $Q = 1.8 \times 10^{-2}$ - e.g. a mono-energetic 4.8 kA 30 MeV proton beam. Such characteristics may be achievable in the near future by

laser-produced proton beams as the individual characteristics can already be separately reached[10]. The initial beam density is radially Gaussian with rms beam width $\sigma_x = 200 \mu\text{m}$ and zero divergence $\sigma'_x = 0$. The foil spacing is set to $L = 100 \mu\text{m}$ and the foil thicknesses Δ_f range from 0 to $12.8 \mu\text{m}$. The initial beam emittance is $\epsilon_{x,\text{rms}} = 0.87 \text{ mm mrad}$. The emittance in this case grows due to foil-induced scattering in the thin, but finite thickness foils. The finite foil thickness induces a reduction of focusing that we quantify by the focusing efficiency defined by

$$\eta(\Delta_f) = \frac{\sigma_{x,\text{init}} - \sigma_{x,\min}(\Delta_f)}{\sigma_{x,\text{init}} - \sigma_{x,\min}(\Delta_f = 0)}. \quad (24)$$

Here, $\sigma_{x,\text{init}}$ is the initial rms beam width. $\sigma_{x,\min}(\Delta_f)$ is the best focus for foils with thickness Δ_f , occurring at a distance z_{\min} after the first foil. z_{\min} is called the effective focal length. The minimum beam rms width for infinitely thin foils is $\sigma_{x,\min}(\Delta_f = 0)$. This definition of the focusing efficiency factor η is valid only when the foil spacing is small enough to induce initial focusing. The focusing efficiency η is desired to be as close as possible to unity, corresponding to small defocusing degradation due to scattering and energy losses. Mitigation of foil-induced scattering can be achieved by reducing the foil thickness Δ_f , the addition of an external focusing system, or using higher initial beam energy \mathcal{E}_b .

The dependence of the focusing efficiency η as a function of foil thickness Δ_f for various initial proton kinetic energies is shown in Fig. 6. The beam rms width σ_x , emittance and energy for various foil thicknesses and an initial beam kinetic energy $\mathcal{E}_b = 30$ MeV are plotted in Fig. 7. The plot of the beam rms width shows that, as expected, thicker foils decrease the maximum beam focus, but are still preferable to the vacuum case where the beam quickly expands. The plot of the axial beam kinetic energy \mathcal{E}_b is consistent with the stopping power of the employed tabulated PSTAR data in Ref [21]. Emittance growth is observed in the plot of the beam emittance. Table I summarizes the beam size and emittance at maximum focusing for a variety of foil thicknesses. Plots of particle-in-cell simulation results obtained from WARP[17] (see Sec. IV) are also included in Figure 7. The focusing efficiency is quickly reduced with thicker foils, which moves the focal spot closer to the entrance of the stack of the thin foils, reduces the beam kinetic energy, and increases the beam emittance. The effects are more deleterious for a beam with lower perveance (i.e., less magnetic focusing) and lower energy (i.e. more scattering and faster kinetic energy loss). For example, a cold 10 MeV proton beam of perveance 8.14×10^{-3} would have a focusing efficiency of 9 % for even an extremely thin foil of thickness $\Delta_f = 160 \text{ nm}$, which means that passive focusing cannot effectively operate for such low energy and low perveance beams. In order to achieve a focusing efficiency of 70 % for such a beam, the foil thickness would have to be about 24 nm. Nonetheless, even though focusing cannot be achieved, the stack of

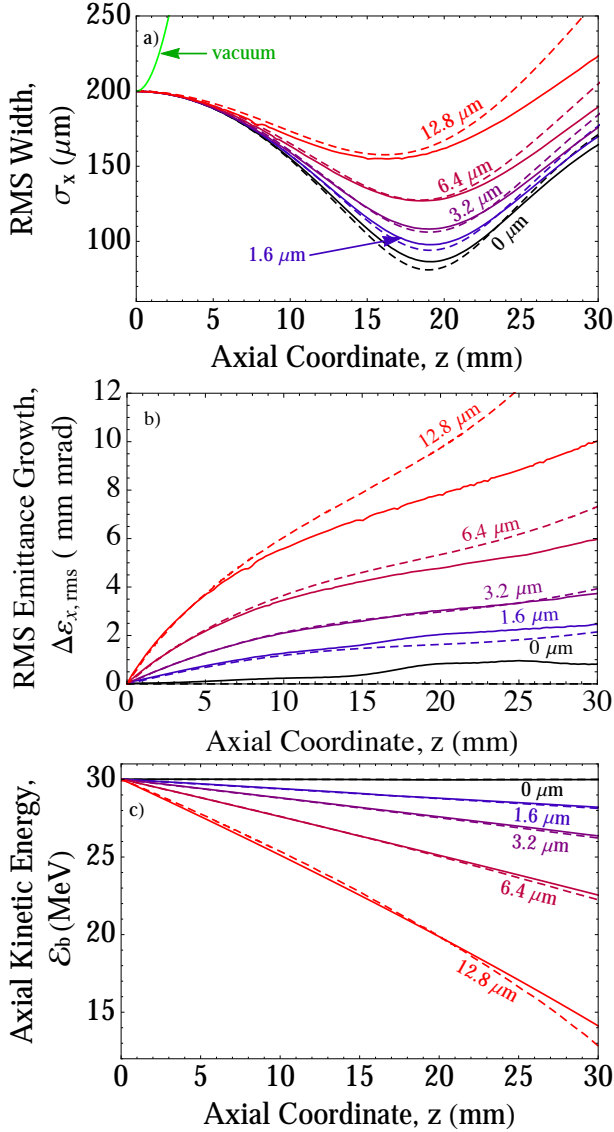


FIG. 7: (Color) The evolution of rms beam width σ_x (a), rms transverse emittance growth $\Delta\epsilon_{x,\text{rms}}$ (b) and axial kinetic energy E_b (c) as a function of z for foil spacing $L = 100 \mu\text{m}$ and foil thickness $\Delta_f = 0, 1.6, 3.2, 6.4, 12.8 \mu\text{m}$ as labeled. Quantities at the focal spot (z position of the smallest σ_x) are summarized in Table. I. Dashed lines represent the envelope model solutions. Solid lines represent WARP simulations.

foils strongly mitigates defocusing compared to vacuum values (see Fig. 7). Results presented here help clarify where idealized results from Ref. [1], in which scattering and energy losses were neglected, can be reliably applied.

Since passive focusing is nonlinear (the focusing term in the envelope equation is proportional to Q/σ_x in contrast to solenoidal focusing that is linear, i.e. proportional to $\kappa\sigma_x$ where κ is the applied focusing function), equivalence in terms of thin lens optics is not possible. Therefore, as an approximate comparison between passive focusing and solenoidal focusing, we com-

pute the necessary solenoidal magnetic field to reach the same minimum spot size $\sigma_{x,\text{min}}$ provided by passive focusing. For the above-mentioned beam parameters, in the absence of foils, a solenoidal magnetic field of 600 T would be required to reach the minimum spot size $\sigma_{x,\text{min}} = 157.6 \mu\text{m}$ that is provided by a stack of thin foils of thickness $\Delta_f = 12.8 \mu\text{m}$. This shows the advantage of foil focusing relative to vacuum focusing with applied fields for the beam parameters examined here. In optimized systems, it may be advantageous to use combined solenoid and foil focusing, using fewer foils and the solenoid strength where the beam is large, and more foils as the beam focuses. This could partly mitigate scattering issues and give more system tunability. Note that, while quadrupoles are also linear optics, their uses are more even problematic. One could indeed superimpose high gradient pulsed magnet quadrupole periodic lattices to replace the solenoid focusing. Estimates show that for an occupancy of 0.5 and the quadrupole length $L = 2$ mm (this short length is required for the effective focal length z_{min} to be in the same range as the study above, i.e. in the tens of mm range), the required magnetic gradient is 6×10^5 T/m, or, equivalently, a field of 30 T for a radius of $50 \mu\text{m}$. These are extreme fields. Alternatively, to avoid those extreme fields, one could use upstream (non-immersed) quadrupole optics in a combined type final focus using permanent magnets, but that also introduces another issue regarding the behavior of electrons respective to the dynamics of ions when entering the quadrupoles.

IV. SIMULATIONS

The envelope model is compared to particle-in-cell simulations using the WARP code[17] in axisymmetric cylindrical (r - z) geometry with a regular grid. The basic simulation model is also discussed in Ref. [1]; it is generalized here to include scattering and energy loss effects. The setup of the present simulations is similar to what was referred as the "infinite beam" simulation setup of Ref [1], and agrees well with its analytical envelope model that excludes scattering and energy loss effects. The domain is bounded radially by the beam pipe at $r = 1.2$ mm and axially by the ends of two adjacent foils, and contains by 64 radial grid cells and 8 axial grid cells. The boundary conditions for macro-particles are absorbing in the r direction and periodic in the z direction. This choice of boundary conditions for particles speeds up the simulation as particles exiting from the right end are reinjected back into the domain from the left end with the same velocity and the same transverse position. This bypasses the need for much larger simulations of the whole stack of thin foils and focuses on the beam dynamics between two foils and within one foil. The electric field is calculated in the electrostatic approximation with Dirichlet boundary conditions in r and in z . The magnetic field is calculated in the magnetostatic approximation with Dirichlet

boundary conditions in r and periodic boundary conditions in z . Beam macro-particles are initially loaded with regular spacing in the z direction.

In the r direction, the particles are loaded following an initially axisymmetric Gaussian charge profile, chopped at $r = r_{\max} = 3.5\sigma_b$. The particles are spaced uniform in R^2 out to $R = r_b = 2\sigma_b$, with R related to the actual radius r by the relation

$$r = \sigma_x \sqrt{-2 \ln \left[1 - \left(\frac{R}{2r_b} \right)^2 \mathcal{N} \right]}. \quad (25)$$

with $\mathcal{N} = 1 - \exp(-r_{\max}^2/(2\sigma_b^2))$, a normalisation factor due to the chopping (see Appendix B for details).

The rms transverse beam size σ_x is computed by averaging over the full axial domain. Typically, 296 macro-particles are loaded per particle-containing cell. These simulated beam parameters are identical to the beam parameters of the envelope model of Sec. III E for direct comparison. Parametric numerical studies in the absence of scattering showed that the grid resolution and statistics were sufficient for well converged simulations[1]. Scattering and energy losses are not expected to change requirements.

Scattering and energy loss options were added to the modeling of foils in WARP. Foils are located at each axial end of the domain and assumed to extend to the radial boundaries. When a particle penetrate a foil, the particle is given a random transverse kick that follows the normal distribution with mean 0 and variance $\langle \theta_x^2 \rangle = G_{\text{SRIM}}^2 \Delta_f / \mathcal{E}_b^2$ [see Eq (7)]. After scattering, the kinetic energy of the beam \mathcal{E}_b is reduced by $\Delta \mathcal{E}_b \simeq \mathcal{S}(\mathcal{E}_b(-\Delta_f/2)) \Delta_f$ [see Eq. (22)].

Results of these simulations are shown in Fig. 7 and agree reasonably well with the envelope results for the axial kinetic energy \mathcal{E}_b . The minor discrepancies between the simulations and the envelope model are due to various effects not included in the envelope model as mentioned in Ref. [1]: (i) the radial density is evolving and does not stay Gaussian, (ii) the electric field is not averaged between the foil by using \bar{F} , and (iii) emittance growth due to the non-linear nature of the self-fields. Thicker foils enhance these differences.

V. REMARKS

This paper generalized recent theory and simulation models in Ref. [1] to include the degradation of beam quality due to foil-induced scattering and energy loss in passive focusing. This study shows that a higher beam kinetic energy, a lower beam atomic number and/or foil thickness are needed for optimal passive focusing using a stack of thin foils. Extending the study to a larger range of foil properties (e.g., with irregular spacing and thickness, different shape, holes) would open possibilities to optimized passive focusing systems for more complex

beams (e.g. with large energy spectrum, not initially collimated, with co-moving and secondary elections).

Acknowledgments

This work was performed under the auspices of the U.S. Department of Energy by Lawrence Livermore National Security, LLC, Grant DE-AC52-07NA27344, and supported at UC Berkeley under Grant DE-FG02-04ER41289.

Appendix A: Calculation of the moments $\langle xw' \rangle$ and $\langle x'w' \rangle$ within metallic foils.

Consider Eq. (14) with constant kinetic energy ($\gamma_b \beta_b = \text{const}$) and in the x direction. By introducing $K = -\frac{q}{m\gamma_b c^2 x} \frac{\partial \phi_w}{\partial x}$, a Hill's equation with a stochastic term is obtained,

$$x''(z) + K(z)x(z) = w'(z), \quad (A1)$$

where w' is white noise that we model as a sum of discrete kicks with

$$w'(z) = \sum_{i=1}^n \Delta_i \delta(z - z_i). \quad (A2)$$

Here, $\delta(z)$ is the Dirac delta function, z_i is the axial position where the i 'th transverse kick occurs, n is the total number of transverse kicks from the axial coordinate $-\Delta_f/2$ to z , and Δ_i the amplitude of the i 'th kick. From Sec. II B, the kicks Δ_i are normal distributed centered on 0 with variance $G^2/\mathcal{E}_b^2(z)\delta z$. Here δz is the mean free path between two collisions. Between two kicks (i.e., for any $z \neq z_i$ with $i \in \llbracket 1, n \rrbracket$), Eq. (A1) reduces to the regular Hill's equation,

$$x''(z) + K(z)x(z) = 0. \quad (A3)$$

The solution of the regular Hill's equation, Eq. (A3), between the i 'th kick and the $(i+1)$ 'th kick has the form

$$x_i(z) = [A_i f_i(z - z_i) + B_i g_i(z - z_i)][H(z - z_i) - H(z - z_{i+1})]. \quad (A4)$$

Here, A_i and B_i are constants that depend on the initial conditions, C_i and S_i are cosine-like and sine-like functions satisfying Eq. (A3) with initial conditions $C_i(0) = 1$, $C'_i(0) = 0$, $S_i(0) = 0$, $S'_i(0) = 1$, and H is a "step" function defined such that

$$H(z) = \begin{cases} 1, & z > 0 \\ \frac{1}{2}, & z = 0 \\ 0, & z < 0. \end{cases} \quad (A5)$$

The general solution of Eq. (A1) can be expressed as

$$x(z) = \sum_{i=0}^n x_i(z). \quad (A6)$$

Consider a particle with initial conditions $x(z_0) = x_0$ and $x'(z_0) = x'_0$ where $z_0 = -\Delta_f/2$. This sets $A_0 = x_0$, $B_0 = x'_0$. Note that $z_i > z_{i-1}$ for $i > 0$. Then, the following equations recursively hold for any $i > 0$:

$$\begin{aligned} A_i &= A_{i-1}C_{i-1}(z_i - z_{i-1}) + B_{i-1}S_{i-1}(z_i - z_{i-1}), \\ B_i &= A_{i-1}C'_{i-1}(z_i - z_{i-1}) + B_{i-1}S'_{i-1}(z_i - z_{i-1}) + \Delta_i. \end{aligned} \quad (\text{A7})$$

It can be shown that, for any $i > 1$,

$$\begin{aligned} A_i &= \mathcal{A}_i + \sum_{j=1}^{i-1} \mathcal{C}_{i,j} \Delta_j, \\ B_i &= \mathcal{B}_i + \sum_{j=1}^{i-1} \mathcal{D}_{i,j} \Delta_j + \Delta_i, \end{aligned} \quad (\text{A8})$$

where \mathcal{A}_i , \mathcal{B}_i , $\mathcal{C}_{i,j}$, $\mathcal{D}_{i,j}$ are constants that depend solely on A_0 , B_0 , and C_i , C'_i , S_i , S'_i evaluated at z_i and z_{i-1} . Their explicit evaluation is not necessary in our analysis.

We can now compute $\langle xw' \rangle$ and $\langle x'w' \rangle$ within the metallic foil. Applying Eq. (A2), Eq. (A4), and Eq. (A8), we first calculate

$$\begin{aligned} \langle xw' \rangle(z) &= \left\langle \sum_{i=1}^n \sum_{k=1}^n \Delta_k (A_i f_i(z_k - z_i) + B_i g_i(z_k - z_i)) \right. \\ &\quad \times (H(z_k - z_i) - H(z_k - z_{i+1})) \delta(z - z_k) \rangle \\ &= \left\langle \frac{1}{2} \sum_{i=1}^n \Delta_i \delta(z - z_i) (\mathcal{A}_i + \sum_{j=1}^{i-1} \mathcal{C}_{i,j} \Delta_j) \right\rangle. \end{aligned} \quad (\text{A9})$$

Because the Δ_i are isotropically distributed, we have

$$\left\langle \sum_{i=1}^n \Delta_i \delta(z - z_i) \mathcal{A}_i \right\rangle = 0, \quad \left\langle \sum_{i=1}^n \Delta_i \delta(z - z_i) \sum_{j=1}^{i-1} \mathcal{C}_{i,j} \Delta_j \right\rangle = 0.$$

In this result, note that for $j < i$, $\Delta_i \neq \Delta_j$ and all terms in the average vanish because there is no quadratic terms in Δ_i^2 in the sums. Together, these results show that

$$\langle xw' \rangle(z) = 0. \quad (\text{A10})$$

Similarly, we compute $\langle x'w' \rangle$ within a metallic foil,

$$\begin{aligned} \langle x'w' \rangle(z) &= \left\langle \sum_{i=1}^n \sum_{k=1}^n \Delta_k (A_i f'_i(z_k - z_i) + B_i g'_i(z_k - z_i)) \right. \\ &\quad \times (H(z_k - z_i) - H(z_k - z_{i+1})) \delta(z - z_k) \rangle \\ &= \left\langle \frac{1}{2} \sum_{i=1}^n \Delta_i^2 \delta(z - z_i) \right\rangle. \end{aligned} \quad (\text{A11})$$

$\left\langle \sum_{i=1}^n \Delta_i^2 \delta(z - z_i) \right\rangle$ in Eq. (A11) is approximated by averaging it over a mean free path δz . Because the Δ_i are normal distributed centered on 0 with variance $G^2/\mathcal{E}_b^2(z)\delta z$,

carrying out this average gives

$$\begin{aligned} \left\langle \sum_{i=1}^n \Delta_i^2 \delta(z - z_i) \right\rangle &\simeq \frac{1}{\delta z} \int_{z-\frac{\delta z}{2}}^{z+\frac{\delta z}{2}} dz \left\langle \sum_{i=1}^n \Delta_i^2 \delta(z - z_i) \right\rangle \\ &\simeq \frac{1}{\delta z} \langle \Delta_n^2 \rangle \\ &\simeq \frac{G^2}{\mathcal{E}_b^2}, \end{aligned} \quad (\text{A12})$$

resulting in

$$\langle x'w' \rangle(z) = \frac{1}{2} \frac{G^2}{\mathcal{E}_b^2}. \quad (\text{A13})$$

Appendix B: Loading in the radial direction of a beam with a radial Gaussian profile on a the (r - z grid)

Transversely, the beam macro-particles are initially loaded as if the beam radial distribution is axisymmetrically uniform, following the uniform beam radial density

$$\rho_{b,\text{uni}}(R) = \begin{cases} \frac{\lambda}{\pi} \frac{1}{r_b^2}, & 0 \leq R \leq r_b, \\ 0, & r_b < R. \end{cases} \quad (\text{B1})$$

The number of particles therefore scales as R^2 in the (R - z) grid. Then, the radial coordinate R of each of the macro-particles is mapped to the new coordinate r to obtain a Gaussian distribution in the physical (r - z) grid chopped at $r = r_{\text{max}}$ using the formula

$$\int_0^r \rho_{b,\text{gau}}(\tilde{r}) 2\pi \tilde{r} d\tilde{r} = \int_0^R \rho_{b,\text{uni}}(\tilde{R}) 2\pi \tilde{R} d\tilde{R} \quad (\text{B2})$$

where

$$\rho_{b,\text{gau}}(r) = \begin{cases} \frac{\lambda}{\pi} \frac{1}{2\sigma_b^2} \left[\exp\left(-\frac{r^2}{2\sigma_b^2}\right) / \mathcal{N} \right], & 0 \leq r \leq r_{\text{max}}, \\ 0, & r_{\text{max}} < r \end{cases} \quad (\text{B3})$$

is the Gaussian radial density chopped at r_{max} . $\mathcal{N} = 1 - \exp(-r_{\text{max}}^2/(2\sigma_b^2))$ is a normalisation factor to account for the chopping. Eq. (B2) yields an explicit expression for

$$r = \sigma_b \sqrt{-2 \ln \left[1 - \left(\frac{R}{2r_b} \right)^2 \mathcal{N} \right]}. \quad (\text{B4})$$

Note that $r_b = 2\sigma_b$ as both values are rms-equivalent beam radii[1].

- (John Wiley & Sons, New York, 1994).
- [3] J. J. Barnard and S. M. Lund, U.S. Particle Accelerator School courses: *Beam Physics with Intense Space-Charge*, Hampton, VA, 19-30 January 2015, <https://people.nscl.msu.edu/~lund/uspas/bpisc.2015/>.
 - [4] C. L. Olson, *Physics of Fluids* **16**, 529 (1973).
 - [5] J. Hasegawa, K. Kondo, Y. Oguri, and K. Horioka, *Nuclear Instruments and Methods in Physics Research Section A: Accelerators, Spectrometers, Detectors and Associated Equipment* **733**, 32 (2014).
 - [6] R. F. Fernsler, R. F. Hubbard, and S. P. Slinker, *J. Appl. Phys.* **68**, 5985 (1990).
 - [7] E. Henestroza, B. G. Logan, and L. J. Perkins, *Phys. Plasmas* **18**, 032702 (2011).
 - [8] G. Caporaso, S. Sampayan, Y.-J. Chen, J. Harris, S. Hawkins, C. Holmes, M. Krogh, S. Nelson, W. Nunnally, A. Paul, et al., *Nuclear Instruments and Methods in Physics Research Section B: Beam Interactions with Materials and Atoms* **261**, 777 (2007).
 - [9] J. Barnard, J. Armijo, D. Bailey, A. Friedman, F. Bieniosek, E. Henestroza, I. Kaganovich, P. Leung, B. Logan, M. Marinak, et al., *Nuclear Instruments and Methods in Physics Research Section A: Accelerators, Spectrometers, Detectors and Associated Equipment* **606**, 134 (2009).
 - [10] A. Macchi, M. Borghesi, and M. Passoni, *Rev. Mod. Phys.* **85**, 751 (2013), URL <http://link.aps.org/doi/10.1103/RevModPhys.85.751>.
 - [11] S. Wilks, A. Langdon, T. Cowan, M. Roth, M. Singh, S. Hatchett, M. Key, D. Pennington, A. MacKinnon, and R. Snavely, *Physics of Plasmas* (1994-present) **8**, 542 (2001).
 - [12] P. Ni, B. Logan, S. Lund, N. Alexander, F. Bieniosek, R. Cohen, M. Roth, and G. Schaumann, *Laser and Particle Beams* **31**, 81 (2013).
 - [13] P. A. Ni, S. M. Lund, C. McGuffey, N. Alexander, B. Aurand, J. J. Barnard, F. N. Beg, C. Bellei, F. M. Bieniosek, C. Brabetz, et al., *Physics of Plasmas* **20**, 083111 (pages 6) (2013).
 - [14] G. Penn and J. Wurtele, *Phys. Rev. Lett.* **85**, 764 (2000).
 - [15] K.-J. Kim and C.-X. Wang, *Phys. Rev. Lett.* **85**, 760 (2000).
 - [16] J. F. Ziegler, M. Ziegler, and J. Biersack, *Nuclear Instruments and Methods in Physics Research Section B: Beam Interactions with Materials and Atoms* **268**, 1818 (2010).
 - [17] A. Friedman, R. H. Cohen, D. P. Grote, S. M. Lund, W. M. Sharp, J.-L. Vay, I. Haber, and R. A. Kishek (2013), URL <http://warp.lbl.gov/>.
 - [18] J. D. Jackson, *Classical Electrodynamics* (John Wiley & Sons, New York, 1998), 3rd ed.
 - [19] M. J. Berger, J. Coursey, M. Zucker, and J. Chang, *Stopping-power and range tables for electrons, protons, and helium ions* (NIST Physics Laboratory, 1998).
 - [20] R. Hubbard, S. Goldstein, and D. Tidman, in *Heavy Ion Fusion Workshop* (1979), p. 488.
 - [21] M. Z. M. J. Berger, J.S. Coursey and J. Chang, NIST, Physical Measurement Laboratory (1992).
 - [22] S. M. Lund and B. Bukh, *Phys. Rev. ST – Accel. Beams* **7**, 024801 (2004).